

RESEARCH

Open Access



Lithium-doped calcium silicate cement regulates the immune microenvironment and promotes M2 macrophage polarization for enhancing bone regeneration

Yen-Hong Lin^{1,2†}, Cheng-Yu Chen^{2†}, Kun-Hao Chen³, Ting-You Kuo⁴, Tsung-Li Lin^{5,6*} and Ming-You Shie^{1,2,7*}

Abstract

Bone defects present a significant challenge in orthopedics and trauma surgery, necessitating innovative approaches to stimulate effective bone regeneration. This study investigated the potential of lithium-doped calcium silicate (LiCS) cement to enhance bone regeneration and modulate the immune microenvironment to promote tissue repair. We synthesized a LiCS ceramic powder and performed comprehensive analyses of its physicochemical properties, including phase composition, morphology, setting time, and mechanical strength. The results demonstrated that the incorporation of lithium into calcium silicate significantly increased the diametral tensile strength (DTS) and facilitated hydroxyapatite formation compared with undoped calcium silicate. In vitro assays revealed that the LiCS cement enhanced the proliferation, adhesion, and spread of Wharton's jelly mesenchymal stem cells (WJMSCs). Additionally, Li-CS cement exhibited remarkable immunomodulatory properties by reducing pro-inflammatory cytokines and increasing anti-inflammatory cytokines, promoting the polarization of macrophages towards the M2 phenotype. The presence of Li in the cement also significantly improved the osteogenic differentiation of WJMSCs, as evidenced by elevated levels of alkaline phosphatase and osteocalcin expression. These findings underscore the dual functional capabilities of the LiCS cement in enhancing osteogenesis and modulating the immune environment, making it a promising material for bone tissue engineering and regeneration.

Keywords Lithium, Calcium silicate, Bone regeneration, Immune modulation, Macrophage polarization, Osteogenesis

[†]Yen-Hong Lin and Cheng-Yu Chen contributed equally to this work.

*Correspondence:

Tsung-Li Lin
alilin422@yahoo.com.tw
Ming-You Shie
eric@mail.cmu.edu.tw

¹Department of Biomedical Engineering, China Medical University, Taichung 406040, Taiwan

²Research & Development Center for x-Dimensional Extracellular Vesicles, China Medical University Hospital, Taichung 404332, Taiwan

³School of Medicine, China Medical University, Taichung 406040, Taiwan

⁴Graduate Institute of Biomedical Sciences, China Medical University, Taichung 406040, Taiwan

⁵Department of Sports Medicine, College of Health Care, China Medical University, Taichung 406040, Taiwan

⁶Department of Orthopedics, China Medical University Hospital, Taichung 404332, Taiwan

⁷Department of Bioinformatics and Medical Engineering, Asia University, Taichung 41354, Taiwan



© The Author(s) 2024. **Open Access** This article is licensed under a Creative Commons Attribution-NonCommercial-NoDerivatives 4.0 International License, which permits any non-commercial use, sharing, distribution and reproduction in any medium or format, as long as you give appropriate credit to the original author(s) and the source, provide a link to the Creative Commons licence, and indicate if you modified the licensed material. You do not have permission under this licence to share adapted material derived from this article or parts of it. The images or other third party material in this article are included in the article's Creative Commons licence, unless indicated otherwise in a credit line to the material. If material is not included in the article's Creative Commons licence and your intended use is not permitted by statutory regulation or exceeds the permitted use, you will need to obtain permission directly from the copyright holder. To view a copy of this licence, visit <http://creativecommons.org/licenses/by-nc-nd/4.0/>.

Introduction

Bone defects represent a significant challenge in the fields of orthopedics and trauma surgery, posing a substantial obstacle to the natural healing process owing to their extensive size and complexity [1]. Such a defect is defined as a bone lesion or gap that cannot heal spontaneously within a patient's lifetime, necessitating interventions to restore function and structure [2]. These defects often result from traumatic injuries, tumor resection, congenital anomalies, or surgical interventions, and their management requires innovative approaches to effectively stimulate bone regeneration [3]. The pathophysiology of critical-size bone defects is underpinned by an imbalance between bone formation and resorption, where natural healing mechanisms, including the recruitment of osteoprogenitor cells and the subsequent bone remodeling process, are insufficient to mitigate the defect [4–6].

The interplay between the immune system and bone regeneration highlights the importance of creating a conducive osteoimmune environment [7–9]. This environment, shaped by the body's response to biomaterial implantation, is characterized by an intricate balance between immune cell infiltration and cytokine profiles, which fundamentally guides the outcome of bone healing [10]. Macrophages, which are pivotal in orchestrating this immune response, display remarkable versatility by polarizing into pro-inflammatory (M1) and anti-inflammatory (M2) phenotypes, each playing distinct roles in the progression of osteogenesis [11–13]. The initial inflammatory response, dominated by M1 macrophages, sets the stage for subsequent tissue repair by establishing a specific “immune environment” that is crucial for biomaterial-mediated osteogenesis [14]. However, the transition towards tissue regeneration necessitates a shift towards M2 macrophages, emphasizing the need for a balanced macrophage phenotype transition to effectively suppress inflammation and enable successful bone regeneration [15]. Therefore, understanding the dynamics of the osteoimmune environment offers a promising avenue for optimizing biomaterial design to stimulate osteogenesis [16]. By targeting macrophage polarization through biomaterials, it is possible to modulate the immune environment towards a regenerative phenotype, enhance osteointegration, and mitigate disease progression.

The advent of calcium silicate (CS) in the field of bone grafting represents a paradigm shift that addresses the limitations inherent in traditional bone graft materials [17–19]. The pivotal role of CS in promoting enhanced osteogenic and angiogenic responses is crucial for successful bone regeneration [20]. Unlike conventional grafting materials, which offer limited bioactivity and often compromise bone healing, calcium silicate-based materials exhibit superior bioactive properties, which are primarily attributed to the release of soluble silicon ions

[21–23]. These ions stimulate the expression of genes associated with osteoblast differentiation and vascular formation, thereby facilitating the repair of critically sized bone defects [24]. Moreover, CS supports the deposition of a bone-like apatite layer on its surface when immersed in body fluids, further enhancing osteoconductivity [25]. This feature is crucial for integrating the bone cement with the surrounding bone tissue and ensuring the structural and functional restoration of the defect site.

Lithium (Li), a versatile element traditionally used to treat mental health disorders, has emerged as a promising osteogenic agent for bone tissue engineering [26–28]. Its application in enhancing bone regeneration is based on its biochemical influence on osteogenesis [12]. Specifically, the action mechanism of Li includes the inhibition of glycogen synthase kinase-3 β (GSK-3 β), stabilizing β -catenin, and subsequently activating the Wnt signaling pathway, crucial for the promotion of bone growth and repair [29]. The incorporation of Li into bioceramics significantly enhances their osteoinductive properties, leading to improved bone repair outcomes. Li-doped bioceramics support the proliferation and differentiation of osteoblasts and exhibit enhanced degradation properties [30]. These features are vital for the effective regeneration of bone tissue in both *in vitro* and *in vivo* models. Moreover, physicochemical modifications induced by Li doping, such as increased surface roughness, have been identified as beneficial for promoting cell adhesion and proliferation and further facilitating bone tissue formation [31].

In this study, we investigated the efficacy of lithium-doped calcium silicate bone cement (Li-CS) not only in enhancing bone regeneration within bone defects but also in modulating the osteoimmune environment to support tissue repair (Fig. 1). The objective of this study was to evaluate the physicochemical properties and osteoinductive potential of Li-CSs along with their ability to orchestrate immune responses conducive to bone tissue formation and repair. By integrating osteoimmunomodulation into the bone cement design, we aimed to leverage the role of the immune system in bone healing, focusing on the bone cement's capacity to influence macrophage polarization towards a regenerative phenotype. This approach underscores the dual significance of bone cement-mediated osteogenesis and immune regulation for achieving successful bone regeneration.

Materials and methods

Synthesis of LiCS ceramic powder

The synthesis of bioceramic materials via sintering has been described previously [32]. Initially, reagent-grade SiO₂, CaO, Al₂O₃, and Li₂O (all procured from Sigma-Aldrich, St. Louis, MO, USA) were combined as foundational matrix materials with the following composition:

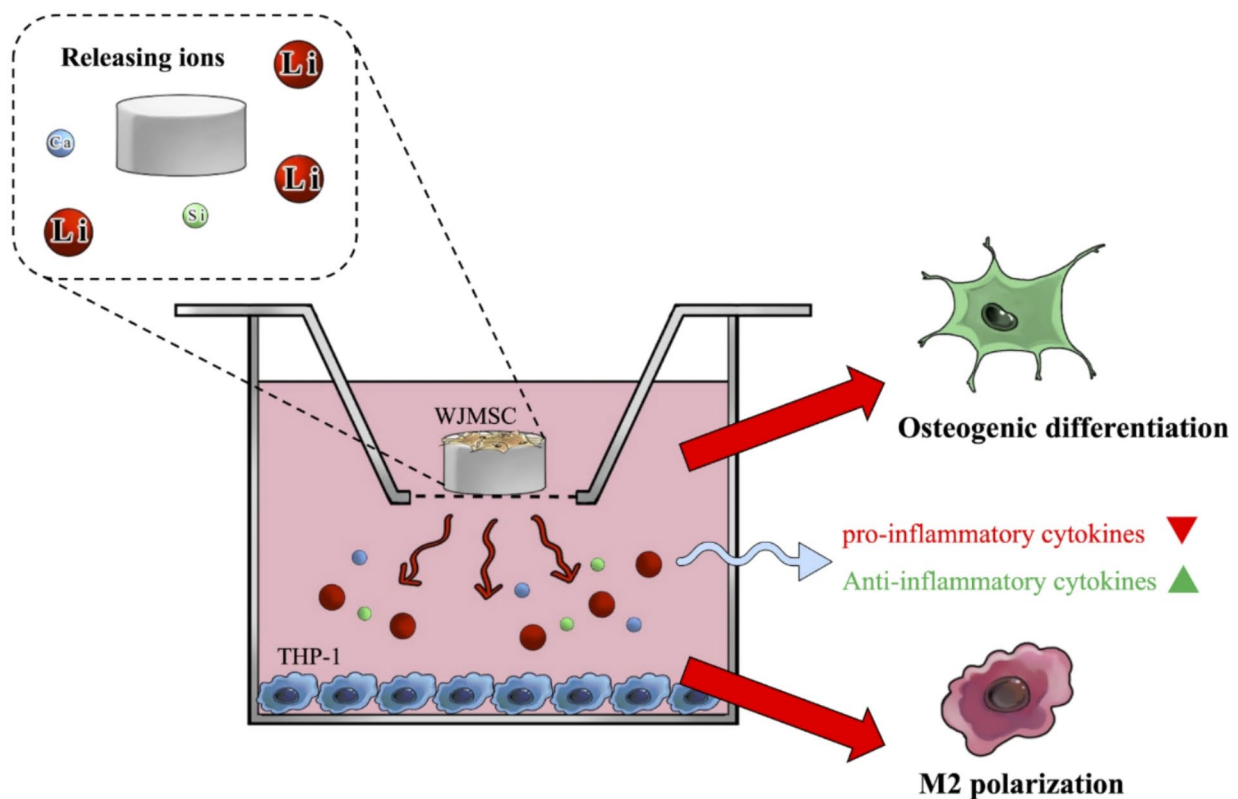


Fig. 1 Schematic diagram of the LiCS cement and the release of ions affecting macrophage in polarization and WJMSCs in osteogenesis

Table 1 Composition (wt%), liquid-to-powder ratio (L/P), and setting time (Ts) of the Ca-Si-Li cement

Code	CaO	SiO ₂	Al ₂ O ₃	LiO	L/P (mL/g)	Ts (min)
Li0	65	30	5	0	0.35	16.0±1.7
Li5	60	30	5	5	0.33	14.6±1.9
Li10	55	30	5	10	0.32	11.9±2.2

CaO+Li₂O (65%), Al₂O₃ (5%), and SiO₂ (30%). The specific nominal weight proportions are listed in Table 1. These oxide mixtures were thoroughly homogenized in anhydrous ethanol and subjected to ball milling at 300 rpm for an extended period overnight using a centrifugal ball mill (Retsch PM100, Germany). Subsequently, these mixtures were relocated to an oven where they were subjected to a controlled temperature ramp of 10°C/min up to a sintering temperature of 1,400°C. The powders were then sintered at the apex temperature for 2 h. After sintering, the products were cooled in a furnace and then ball-milled at 300 rpm for 6 h to achieve the desired fineness. The resulting sintered powder was amalgamated with water, adhered to a predefined liquid-to-powder ratio (as specified in Table 1), and subsequently cast into Teflon molds with a diameter and height of 6 mm and 3 mm, respectively. Previous experimental results indicate that an elevated liquid-to-powder ratio confers a mushy texture to the CS material, thereby

impeding its ability to solidify. All fabricated samples were then incubated at 100% relative humidity and maintained at a temperature of 37°C for a 24-h hydration period.

Phase composition analysis

The phase composition of the cement was meticulously analyzed using an X-ray diffractometer (XRD, Bruker D8 SSS; Bruker Corporation, Karlsruhe, Germany), operating within the 2θ range of 20° to 50°. The device settings were standardized at 30 kV and 30 mA with a scanning speed of 1°/min. This analysis aimed to identify and quantify the various crystalline phases present in cement.

Morphology examination

The microscopic morphology of the cement specimens was examined using field-emission scanning electron microscopy (FE-SEM; JEOL JSM-7800 F; JEOL Ltd., Tokyo, Japan). Observations were conducted in the lower

secondary electron image mode at an accelerating voltage of 3 kV. Additionally, an energy-dispersive spectrometer (EDS) attached to the FE-SEM facilitated the elemental mapping of the specimen surfaces, providing valuable insights into the compositional heterogeneity of the material.

Determination of the setting time

The setting time of the cement was evaluated after mixing the powder with the liquid and placing it in a cylindrical mold. This mold was then stored in an incubator set at 37°C and 100% relative humidity for hydration. Gilmore needles (453.6 g) were used in accordance with the International Standards Organization 9917-1 guidelines for powder/liquid acid-base cements. The setting time was defined as the point at which the needle could not create a 1-mm deep indentation in three separate areas of the cement.

Assessment of mechanical strength

The mechanical strength of the specimens was assessed after a hydration period of 1 d under conditions of 37°C and 100% humidity. Diametral tensile strength (DTS) was measured using an EZ-Test machine (Shimadzu Corp., Kyoto, Japan) capable of applying a force up to 1,000 Newtons at a loading rate of 1 mm/min until failure. The DTS value was calculated using the formula $DTS = 2F/\pi dh$, incorporating the maximum load endured by the specimen (F , in Newtons), the diameter (d , in mm), and the thickness (h , in mm) of the cement. Compressive strength was also assessed using the EZ-Test machine, which was defined as $P/\pi r^2$, where P is the peak load at failure (in Newtons) and r is the radius of the cement specimen. All tests aimed at quantifying the resistance of the cement to mechanical stresses were performed in sextuplicate for each experimental group to ensure the reliability and reproducibility of the results.

Macrophage culture and differentiation

The human acute monocytic leukemia (THP-1) cell line was maintained in the RPMI 1640 medium supplemented with 10% fetal bovine serum, 10 mM HEPES, 1 mM sodium pyruvate, and 100 nM penicillin/streptomycin at 37°C in a humidified incubator with 5% CO₂. For macrophage differentiation, 5×10^5 cells/mL were seeded in fresh RPMI 1640 medium containing 100 ng/mL phorbol 12-myristate 13-acetate (PMA, Sigma) in a 24-well plate. Adherent cells were washed twice with the culture medium (without PMA) and incubated for an additional 24 h to obtain resting macrophages.

Identification of polarized macrophages

To assess the effect of LiCS cement on macrophage polarization, the cement was placed in the upper chamber of a

Transwell insert, whereas THP-1-derived macrophages were cultured in the lower chamber. Polarization of THP-1-derived macrophages into M0, M1, and M2 phenotypes was verified by flow cytometry using phycoerythrin (PE)- and fluorescein isothiocyanate (FITC)-labeled antibodies. Macrophages were carefully scraped and placed in fluorescence-activated cell sorting (FACS) tubes for staining after cleaning in phosphate-buffered saline (PBS). M1 macrophages were identified using CD86 (PE) markers, whereas M2 macrophages were discriminated using CD280 (FITC) markers. After staining, the cells were examined using a BD Accuri C6 Plus flow cytometer (BD Biosciences). Each sample was evaluated using a minimum of 10,000 recorded events. Data analysis was performed using specialized software provided by BD Biosciences. Isotype-matched controls served as baseline references for comparison, with a typical allowance of less than 2% positive cells beyond the established thresholds in the controls. In order to assess ionic release from the cements, the medium was collected and measured the amounts of Ca, Si, and Li ions by using inductively coupled plasma optical emission spectrometer (ICPAES; PerkinElmer OPT 1MA 3000DV, Shelton, CT, USA).

Cell viability

The viability of Wharton's jelly mesenchymal stem cells (WJMSCs) was assessed using the PrestoBlue assay. Initially, the specimens were sterilized by immersion in 75% alcohol and subjected to ultraviolet light irradiation for 30 min in a sterile cabinet. After sterilization, the specimens were washed with PBS and prepared for cell seeding. The cells were directly seeded onto the surfaces of the cement specimens at a density of 5×10^4 cells/mL. These specimens were then cultured in an incubator at 37°C with a humidified atmosphere of 5% CO₂. The culture medium was refreshed every two days. Over various culturing periods, cell cytotoxicity was continuously and repeatedly evaluated using the PrestoBlue® reagent, which measures mitochondrial activity. After cultivation, the medium was discarded, and the wells were washed twice with PBS. Each well was then filled with 30 µL of PrestoBlue® solution and 300 µL of DMEM, followed by incubation at 37°C for 30 min. The assay mixture from each well was subsequently transferred to a new 96-well plate for spectrophotometric analysis at 570 nm with a reference wavelength of 600 nm using a multi-well spectrophotometer (Hitachi, Tokyo, Japan). Cells cultured directly on the plates without cements were used as controls.

Cell morphology

After one, three, and seven days of culture, the cements seeded with WJMSCs were rinsed with PBS and fixed with 4% paraformaldehyde (Sigma-Aldrich) for 15 min. The

cements were immersed in PBS containing 0.1% Triton X-100 (Sigma-Aldrich) to permeabilize the cell membranes. Subsequently, the specimens were incubated with phalloidin (Alexa Fluor 488; Invitrogen) for 1 h to stain the F-actin cytoskeleton. The solution was then discarded, and the cell nuclei were stained with 300 nM DAPI (Invitrogen) for 30 min. Dried specimens were observed under a confocal microscope (Leica TCS SP8; Leica Microsystems, Wetzlar, Germany).

10 cytokine and enzyme activity assays

WJMSCs were cultured at a density of 5×10^4 cells/well on the LiCS cements in 6-well plates. After incubation for 24 h, the culture medium was replaced with a differentiation medium. To evaluate the concentrations of interleukin-1 beta (IL-1 β), interleukin-6 (IL-6), and interleukin-10 (IL-10), as well as the activities of alkaline phosphatase (ALP) and osteocalcin (OC) expression, enzyme-linked immunosorbent assay (ELISA) kits (Invitrogen) were used according to the manufacturer's protocols. The concentrations of IL-1 β , IL-6, and IL-10 in the supernatants were measured after one and three days. ALP activity was assessed on days three and seven by lysing the cells in NP40 cell lysis buffer and centrifuging at 6000 rpm for 15 min using a pNPP ALP assay kit (Bioassay Systems). Total protein content was measured using a bicinchoninic acid (BCA) protein detection kit (Invitrogen), and the relative ALP activity was calculated as the ratio of ALP absorbance to the total protein content. The OC levels were determined using an ELISA kit (Invitrogen) after 7 and 14 days of cultivation, and increased OC levels were observed in the Li5 and Li10 groups after 14 days. Cytokine concentrations and enzyme activities were determined in triplicates from six separate experiments for each condition tested.

11 mineralization assay

After 7 and 14 days of cell culture, as described previously, the specimens were washed several times with PBS and fixed with 4% paraformaldehyde (Sigma-Aldrich) for 15 min. Subsequently, they were stained with 0.5% Alizarin Red S (Sigma-Aldrich) at pH 4.0 for 15 min and then examined with an upright fluorescence microscope (BX53, Olympus, Tokyo, Japan) at 200 \times magnification. The cells were then rinsed with PBS and immersed in 20% methanol and 10% acetic acid to dissolve the staining dye deposited on calcium. The dissolved dye was transferred to a new 96-well plate and quantified using a spectrophotometer at 450 nm. Both staining and quantitative analyses were conducted using six independent samples.

Statistical analysis

One-way analysis of variance was used to assess significant differences between groups, and Scheffé's multiple comparison test was used for each specimen. $P < 0.05$ was considered statistically significant.

Results and discussion

Characterization of cement specimens

The X-ray diffraction (XRD) patterns of the Li-substituted cement specimens are depicted in Fig. 2A. The diffraction patterns of the Li0, Li5, and Li10 samples exhibited distinct peaks indicative of various crystalline phases. For Li0, the dominant peaks are marked by symbols corresponding to CS phases, dicalcium silicate (C_2S) and tricalcium silicate (C_3S), noted predominantly at 2θ values such as $C_2S = 21.9^\circ, 29.6^\circ, 32.7^\circ, 47.6^\circ$, and $C_3S = 31.2^\circ$ and 34.2° [33]. The Li5 and Li10 samples showed a shift in peak intensities with additional peaks at $Li_2SiO_3 = 32.8^\circ$ and 43.2° and $Li_2Si_2O_5 = 23.9^\circ, 37.4^\circ, 39.3^\circ$, and 45.7° , which were identified with Li silicate phases. These changes suggested the incorporation of Li into the

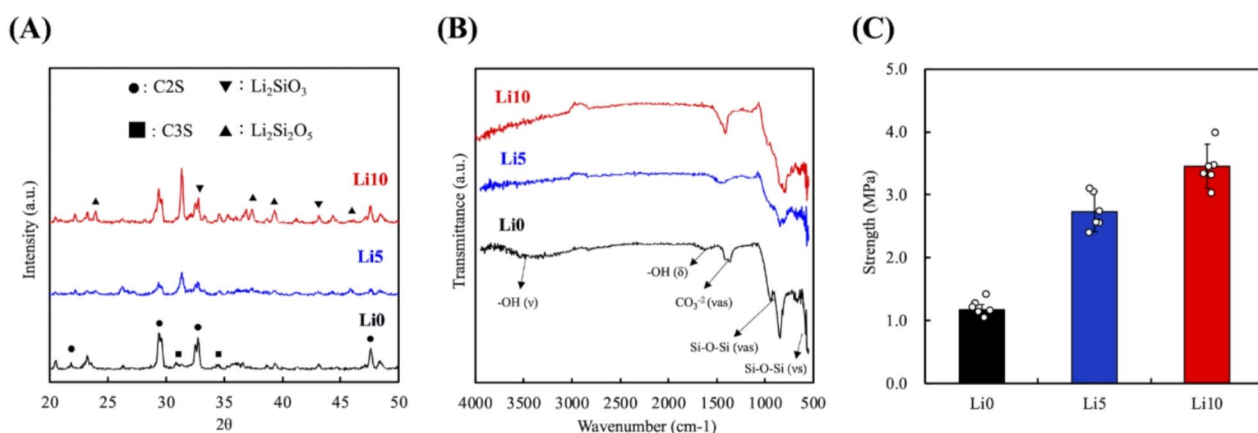


Fig. 2 (A) XRD patterns, (B) FTIR spectra, and (C) Diametral tensile strength (DTS) of calcium silicate cement with different lithium contents (Li0, Li5, and Li10)

cement matrix, which likely altered the silicate network. In addition, the setting times of LiCS cement are listed in Table 1. The setting time of LiCS cement was shortened with increased Li content that showed a setting time ranging from 16.0 ± 1.7 min (Li0) to 11.9 ± 2.2 min (Li10). Li addition was indicated to enhance the hydration processing by accelerating the rupture of the hydration protective film, improving the hydration and the early strength of the cement [34]. A suitable setting time would give the orthopedic surgeon more operation time [35]. Zhao et al. developed calcium silicate cement with initial setting times of over 1 h, which was too long for clinical applications [36].

Selected infrared spectra of LiCS with varying Li contents after hydration are presented in Fig. 2B. The spectra show characteristic absorption peaks, which provide insights into the chemical structure and bonding of the materials. The broad absorption bands around 3300 cm^{-1} in all three spectra were attributed to the stretching vibrations of the O–H bond, indicating the presence of hydroxyl groups or adsorbed water. At approximately 1625 cm^{-1} , a distinct absorption peak was observed assigned to the bending vibration of H–O–H, which was associated with the interlayer water molecules. This peak was present in all three samples, indicating that the incorporation of Li did not significantly affect the amount of interlayer water. The absorption bands around 1416 cm^{-1} were attributed to the asymmetric stretching vibrations of CO_3^{2-} groups, indicative of the presence of carbonate compounds such as calcium carbonate. These peaks were observed in all spectra, suggesting that carbonation occurred regardless of the Li content. Notable peaks around near 941 cm^{-1} corresponded to the asymmetric stretching vibrations of Si–O–Si bonds, which are characteristic of the silicate structure in calcium–silicate–hydrate. These peaks were slightly less intense in the Li10 sample, suggesting some degree of structural modification with higher Li content. Additionally, the absorption bands at approximately 850 cm^{-1} , observed prominently in the Li0 and Li5 spectra, were related to the symmetric stretching vibrations of Si–O–Si bonds. The presence and intensity of these bands across all the spectra indicate that the fundamental silicate structure remained intact with the addition of Li. These bands diminished in intensity with increasing Li content, indicating potential structural changes or reduced polymerization of the silicate network in the presence of Li. In summary, the infrared spectra indicate that the addition of Li to calcium silicate hydrate affects the hydroxyl and carbonate contents as well as the silicate network structure.

Figure 2C shows the DTS values of the hardened calcium silicate samples with varying Li contents. DTS values indicate the mechanical strength of the samples under tension, which is a critical property in structural

applications. The DTS values for the control sample without Li (Li0) were approximately 1.17 ± 0.08 MPa. Incorporating 5% Li (Li5) into the calcium silicate significantly increases the DTS to around 2.73 ± 0.32 MPa. This enhancement suggests that Li incorporation strengthens the calcium silicate matrix, likely by improving the bond strength within the material. For the sample with 10% Li (Li10), the DTS value increased further to approximately 3.45 ± 0.35 MPa. This indicates a continuing trend of strength improvement with increasing Li content, suggesting that Li ions play a vital role in enhancing the structural integrity of calcium silicate. Statistical analysis showed that the differences in the DTS values among Li0, Li5, and Li10 were significant ($P < 0.05$). This confirms that the Li content has a significant impact on the mechanical properties of calcium silicate. The significant increase in strength with the addition of Li can be attributed to the formation of new phases or improved crystallinity within the calcium silicate matrix. In summary, the incorporation of Li into calcium silicate significantly enhanced its diametral tensile strength. Li-doped CS exhibited an increase in the DTS values, demonstrating the potential of Li as a reinforcing agent in calcium silicate-based materials.

In vitro immersion experiment

SEM images of calcium silicate cements with varying Li contents at different time points following immersion in SBF are shown in Fig. 3A. On day 0, the Li0 cement showed a relatively smooth surface with minor irregularities, whereas the Li5 and Li10 cements exhibited rough and irregular surfaces. The increased surface roughness of Li5 and Li10 was beneficial for early cellular adhesion and attachment. This is because rough surfaces enhance fibrin entrapment, promote the adhesion of osteogenesis-related cells, and improve the mechanical stability of biomaterials after transplantation [37]. By day one of SBF immersion, spherical apatite clusters began to form on the surfaces of all the cements. These clusters were more pronounced on the Li10 cement, indicating a higher rate of apatite formation. The Li10 cement displayed larger aggregates of apatite, approximately $1 \mu\text{m}$ in diameter, compared to Li0 and Li5. This trend continued on day three, when the Li10 cement showed extensive apatite coverage, suggesting that a larger surface area was available for apatite formation. The Li0 cement exhibited minimal apatite formation over the same period, highlighting the role of Li in promoting surface mineralization. The Li5 cement exhibited intermediate levels of apatite formation, indicating the dose-dependent effect of Li on apatite nucleation and growth. The incorporation of Li into calcium silicate cement significantly enhanced their ability to support hydroxyapatite formation [38]. This is

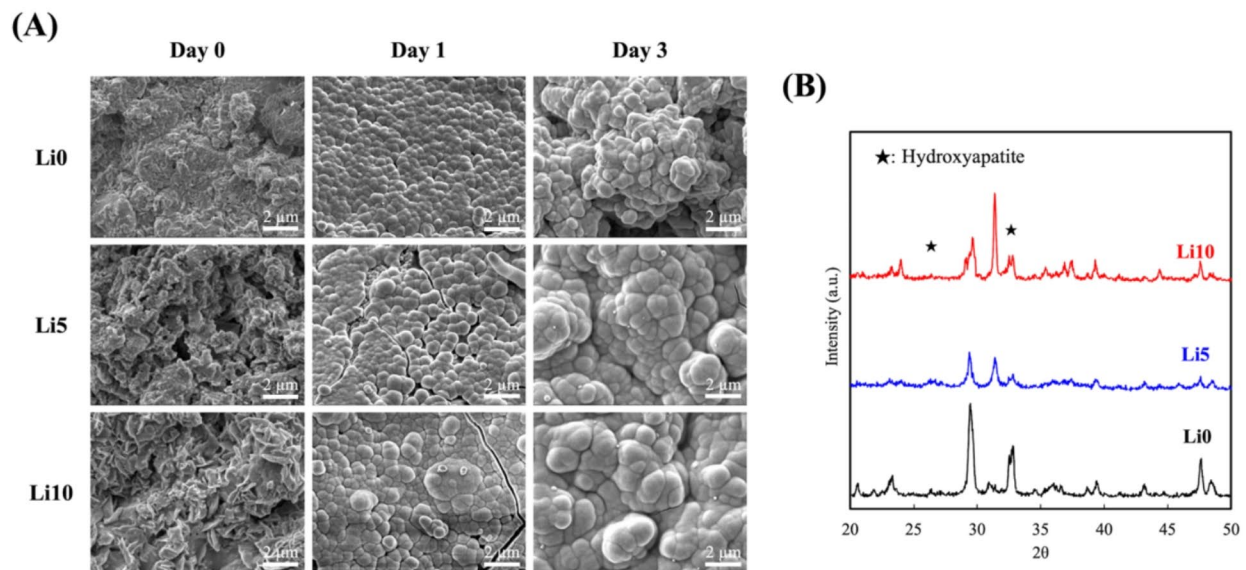


Fig. 3 (A) SEM images of calcium silicate cements with varying lithium contents (Li0, Li5, and Li10) at different time points (Day 0, Day 1, and Day 3) after immersion in simulated body fluid (SBF). (B) The XRD patterns highlight the formation of hydroxyapatite after SBF immersion

consistent with the findings of our previous study, which highlighted the impact of Li on HA formation [39].

The XRD patterns indicate significant changes in the crystalline structure over time. New peaks emerged at approximately 31.8° and 32.7° (marked by asterisks) corresponding to the formation of hydroxyapatite, a biologically relevant phase that suggests potential bioactivity [40]. Interestingly, the Li0 sample showed higher peak intensities than Li5 and Li10, which can be attributed to the larger crystal sizes and higher crystallinity rather than the amount of hydroxyapatite present. Despite the lower peak intensities in the Li5 and Li10 samples, the SEM observations confirmed more extensive hydroxyapatite formation in these samples. This discrepancy suggests that while the Li5 and Li10 cements exhibit more hydroxyapatite coverage and possibly thicker layers, their crystalline domains might be smaller or less crystalline than those of Li0. The incorporation of Li into calcium silicate cements significantly enhanced their ability to support hydroxyapatite formation. The increased surface roughness and larger surface area of the Li5 and Li10 cements promoted better cellular adhesion and faster mineralization. According to Zhang et al., modifications in calcium silicate materials, including the addition of Li, can improve bioactivity and promote the formation of biologically relevant phases, such as hydroxyapatite [41]. Furthermore, the increased hydroxyapatite formation observed in the Li5 and Li10 samples was critical for bone regeneration applications. Hydroxyapatite is known for its excellent biocompatibility and osteoconductivity, rendering it a favorable material for bone repair and regeneration. Materials with a higher hydroxyapatite

content tend to exhibit improved bone bonding and integration [42]. Additionally, the rougher surface morphology observed in the SEM images of the Li5 and Li10 cements was beneficial for osteointegration.

Immunomodulatory capability of LiCS cement

To evaluate the immunomodulatory capability of LiCS cement in vitro, as shown in Fig. 4, the LiCS cement was placed in a transwell system and co-cultured with macrophages. As illustrated in Fig. 4A, the macrophages themselves were derived from monocytes and did not proliferate. No significant differences were noted in cell growth among the groups treated with the Ctl, Li0, Li5, or Li10 cement, and no apoptosis was observed. Hence, the LiCS cement did not exhibit cytotoxicity. To understand the role of the LiCS cement in modulating the immune microenvironment and promoting tissue repair, flow cytometry was used to determine the macrophage phenotype. The levels of pro-inflammatory M1 macrophage-specific marker CD86 (Fig. 4B) and the anti-inflammatory M2 macrophage-specific marker CD280 (Fig. 4C) were measured after two days of culture with LiCS cement. Compared to the Ctl, the expression of CD86 decreased significantly from 35.9 to 25.2% with the addition of Li0 cement. The groups with Li5 and Li10 cements showed further reductions of 17.1% and 15.0%, respectively. In the case of the M2 macrophage-specific marker CD280, the levels in the Ctl group increased from 34.5 to 49.3% with the addition of Li0 cement and further increased to 54.2% and 67.9% in the Li5 and Li10 groups, respectively. After two days of culture, no significant change was noted in the Ctl group, whereas the

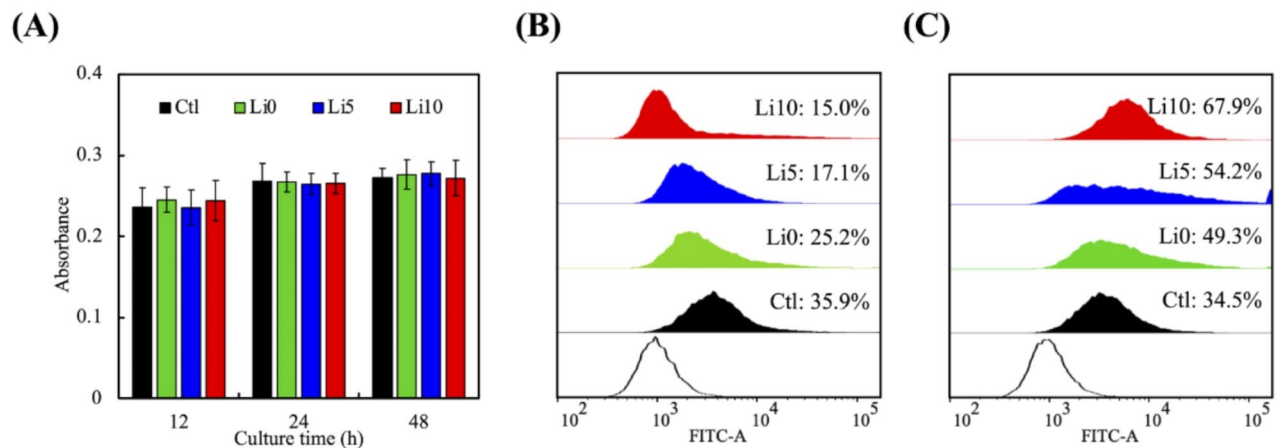


Fig. 4 (A) The growth conditions of macrophages co-cultured with LiCS cement in a transwell system for 12, 24, and 48 h. Expression of (B) M1 macrophage marker CD86 and (C) M2 macrophage marker CD280 after 48 h of co-culture in the transwell system

Table 2 Concentrations of Ca, Si, and Li ions in the medium after culturing for one day

	Ca (mM)	Si (mM)	Li (mM)
Li0	1.35 ± 0.24	2.12 ± 0.21	0.00 ± 0.00
Li5	1.22 ± 0.19	1.98 ± 0.24	0.71 ± 0.12
Li10	1.18 ± 0.18	1.91 ± 0.19	1.33 ± 0.19

addition of Li cement gradually polarized the macrophages towards the M2 phenotype. In the immune systems, macrophages play an important role in immune protection, and a specific macrophage phenotype is necessary for tissue regeneration. In fact, M1 macrophages secrete inflammatory cytokines such as IL-1 β and TNF- α to moderate the inflammatory reaction. In contrast, anti-inflammatory M2 macrophages release pro-tissue repair factors such as IL-10 and TGF- β to stimulate tissue regeneration [43].

Table 2B shows the ion concentrations in the medium after two days. The Si concentrations were approximately 2.12 ± 0.21 mM, 1.98 ± 0.24 mM, and 1.91 ± 0.19 mM for Li0, Li5, and Li10, respectively. In addition, the Li5 and Li10 cement released 0.71 ± 0.12 mM and 1.33 ± 0.19 mM Li ions after two days. In a prior study, Liu et al. confirmed that a culture medium with a Li-ion concentration of less than $14.56 \mu\text{g/mL}$ did not display cytotoxicity [27]. Our results showed that the maximum amount of Li ions released from the Li10 cement was lower than $2.0 \mu\text{M}$, supporting the conclusion that the LiCS cement fabricated in this study did not exhibit cytotoxicity [44]. Immune cells interact with bone regeneration, and this interaction plays a temporary role in the healing process after damage because of sustained high levels of inflammatory factors [45]. WJMSCs cultured with LiCS cement showed reduced expression of TNF- α and IL-1 β and a dose-dependent increase in IL-10 expression [39]. The aforementioned data and research outcomes strongly

demonstrate that Li could dope CS cement with an excellent immune regulatory effect, promoting the polarization of macrophages from a pro-inflammatory phenotype (M1) to a pro-repair phenotype (M2).

Cell proliferation and morphology of WJMSCs cultured on LiCS cement

All the cements displayed a time-dependent increase in cellular proliferation (Fig. 5A). Specifically, the Li10 cement exhibited significantly higher cellular proliferation at each time point (one, three, and seven days) than the Li0 cement ($P < 0.05$). On day seven of culture, Li10 showed the highest absorbance, indicating the highest cell proliferation, followed by Li5 and Li0. The absorbance values of the Li10 and Li5 cements were approximately 20% and 10% higher than those of the Li0. These results suggest that the addition of Li enhances the bioactivity of the calcium silicate cements, promoting better cell proliferation. From the fluorescence staining results (Fig. 5B), we observed more cells on the Li5 and Li10 cements on days three and seven compared to the Li0. Cells on the Li10 cements exhibited extensive spreading and well-defined F-actin microfilaments, indicating good cell adhesion. The surface areas covered by immunofluorescence staining were larger in the Li5 and Li10 groups, suggesting higher cell density and better cell attachment. Morphological analyses indicated that the presence of Li in the cements enhanced cell adhesion and spreading. This observation aligns with previous findings that Li incorporation in biomaterials improved cell-material interactions by increasing hydroxyapatite and providing better cell anchorage points. Additionally, the role of Li in promoting osteogenesis via the activation of RUNX2, a key transcription factor in bone formation has been demonstrated earlier. It may also contribute to enhanced cell adhesion [46]. Li ions can stimulate the Wnt/ β -catenin

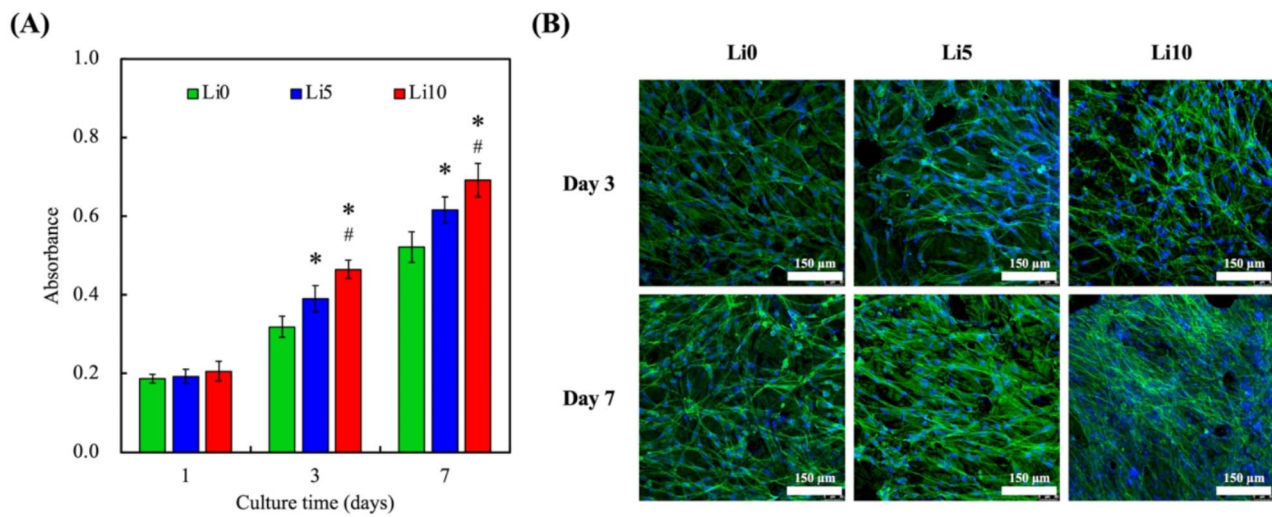


Fig. 5 (A) Cell viability assay results showing the absorbance of calcium silicate scaffolds with varying lithium content (Li0, Li5, and Li10) over one, three, and seven days of culture. Data are presented as the means \pm SEM; $n=6$ for each group. The symbols "*" and "#" denote statistically significant differences ($P<0.05$) between Li5 and Li0 and between Li10 and Li0 groups, respectively. (B) Fluorescent staining images of cells cultured on cements with different lithium content (Li0, Li5, and Li10) on days three and seven, showing cell morphology and distribution. Scale bar: 150 μ m

signaling pathway, which is crucial for cell proliferation and differentiation. This pathway plays a vital role in the maintenance of stem cells and tissue regeneration. The activation of this pathway leads to the accumulation of β -catenin in the cell nucleus, which then triggers the transcription of proliferation-related genes [47].

Inflammatory cytokine and osteogenic marker analysis

Li ions exert anti-inflammatory effects [48]. The levels of inflammatory cytokines, including IL-1 β , IL-6, and IL-10, were analyzed to evaluate the inflammatory response. As illustrated in Fig. 6A, IL-1 β concentration was significantly reduced in the Li10 group compared to the Ctl, Li0, and Li5 groups after one and three days of culture ($P<0.05$). Similarly, IL-6 levels (Fig. 6B) were lower in the Li10 group than in the other groups at both time points ($P<0.05$). This reduction in proinflammatory cytokines suggests the potential of LiCS cements to mitigate inflammation in the context of tissue engineering. Conversely, the anti-inflammatory cytokine IL-10 (Fig. 6C) showed significantly higher expression in the Li10 group than in the other groups after 1 and 3 days of culture ($P<0.05$). The elevated levels of IL-10 further support the hypothesis that the LiCS cements possess anti-inflammatory properties. This anti-inflammatory effect is crucial because inflammation can impair tissue regeneration and the integration of bone grafts [49]. The expression levels of osteogenic markers, including ALP and OC, were evaluated to assess the osteogenic potential of the cements. Figure 6D shows the relative activity of ALP in the cements after three and seven days of culture. Initially, no significant differences were noted in ALP activity across

all groups after three days. However, after seven days, the ALP activity in the Li10 group was significantly higher than that in the Ctl, Li0, and Li5 groups ($P<0.05$). A similar trend was observed for OC concentration (Fig. 6E), where the Li10 group showed the highest levels after 7 and 14 days of culture ($P<0.05$). These results indicate that LiCS cement enhances osteogenic differentiation, rendering it a promising candidate for bone regeneration applications. Additionally, the increase in ALP and OC levels in the Li10 group suggested that Li ions may play a critical role in promoting the differentiation of mesenchymal stem cells into osteoblasts. This is supported by studies showing that Li can activate the Wnt/ β -catenin signaling pathway, which is pivotal for osteogenesis [30]. These results suggested that Li10 cements not only promoted the protein expression of M2 phenotypic polarization but also up-regulated the osteogenic-related protein expression.

After 7 and 14 days of culture, the terminal mineralization of the osteogenic differentiation of WJMSCs was assessed using Alizarin Red S staining for calcium deposition, as illustrated in Fig. 7. On Day 0, the material surfaces are devoid of any cellular presence or mineral deposition, presenting a uniform pinkish background which is indicative of the material's base color before any treatment or cellular activity has taken place. After seven days of growth, it was visually evident that all of the cements had very little calcium accumulation on their surfaces and that the staining intensities were quite similar. However, the dark pink staining on the cement surfaces after 14 days of growth showed that Li5 and Li10 had higher quantities of calcium deposition (Fig. 7A). The

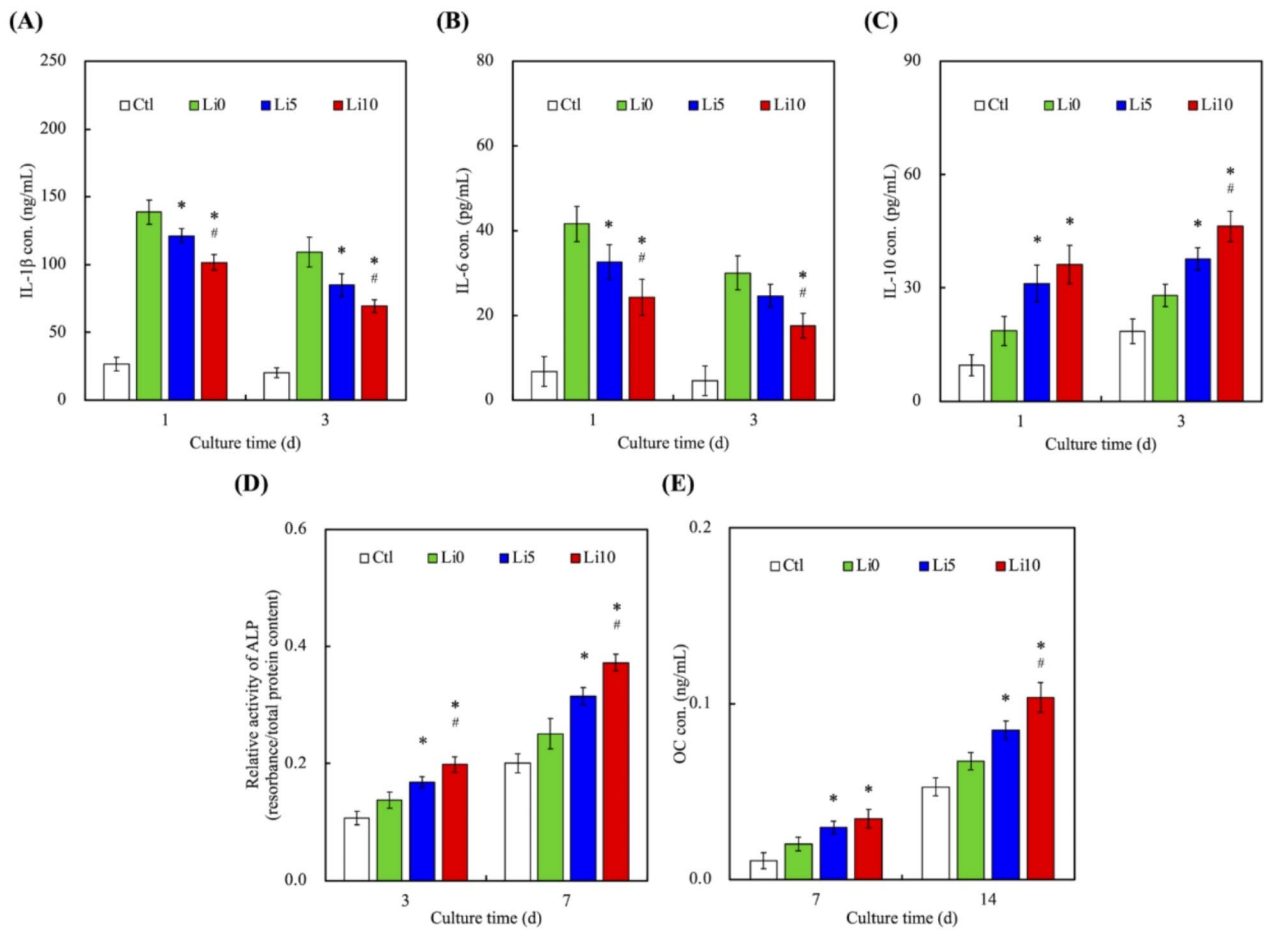


Fig. 6 Analysis of inflammatory and osteogenic markers in samples with different lithium content over various culture times. **(A)** Concentration of interleukin-1 beta (IL-1β) on days one and three, **(B)** Concentration of interleukin-6 (IL-6) on days one and three, **(C)** concentration of interleukin-10 (IL-10) on days one and three, **(D)** relative activity of alkaline phosphatase (ALP) on days three and seven, and **(E)** concentration of osteocalcin (OC) on days 7 and 14. Data are presented as the means ± SEM; *n* = 6 for each group. The symbols "*" and "#" denote statistically significant differences (*P* < 0.05) between Li5 and Li0 and Li10 and Li0 groups, respectively

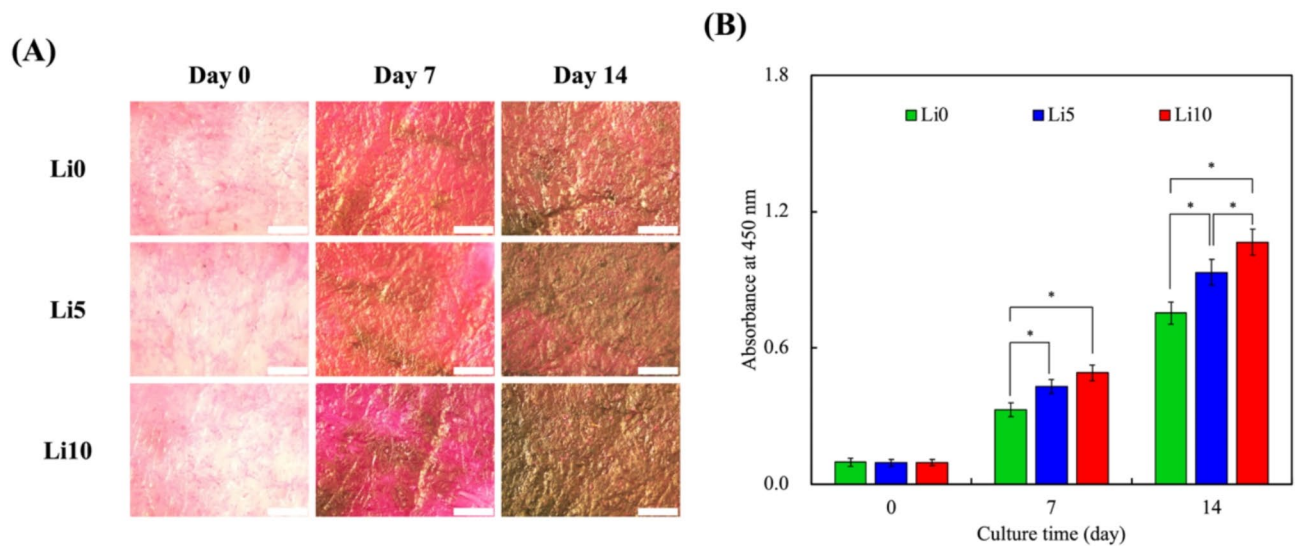


Fig. 7 **(A)** Alizarin Red S staining and **(B)** quantification of calcium mineral deposits by WJMSCs cultured on LiCS cement over different time points. Data are presented as the means ± SEM; *n* = 6 for each group. The symbol "*" denotes statistically significant differences (*P* < 0.05) between the groups

quantitative outcomes (Fig. 7B) corroborated the visual observations and highlighted distinct disparities among the groups at different time points. A significant difference was observed between Li10 and the other groups ($P < 0.05$), highlighting its superior Ca-binding affinity. The inter-group comparison further highlighted a notable difference between Li10 and Li0 ($P < 0.05$), further affirming the enhanced Ca deposition in the presence of Li. Expanding the purview to the 14-day data, Li10 exhibited sustained superiority in Ca mineralization, maintaining significant differences from all other groups. Furthermore, comparative analysis accentuated the distinguishing Ca affinity of Li10 over Li5 and Li0 ($P < 0.05$), which is consistent with the observed hierarchical staining intensities. Therefore, the anti-inflammatory properties observed in the Li10 group may mitigate the adverse effects of chronic inflammation, which is a common challenge in cement-based therapies. LiCS cement can not only enhance the expression of early osteogenic-related proteins but also increase mineralization, which may be associated with the polarization of M2 macrophages under Li ion stimulation and then the BMP2 secretion that stimulates osteogenesis differentiation through the Smad signaling pathway [50]. Therefore, the enhanced osteogenic differentiation suggests that LiCS cement can accelerate bone healing, promoting a more conducive environment for tissue regeneration.

Conclusion

This study explored the innovative integration of LiCS cement to synergize its osteogenic and immunomodulatory capabilities for enhanced bone regeneration. Li, a known stimulator of osteogenesis, and calcium silicate, which is known for its superior bioactivity, were strategically combined to create a composite with exceptional properties. Our findings revealed that LiCS cement not only significantly increased the diametral tensile strength and promoted rapid hydroxyapatite formation but also demonstrated remarkable bioactivity by enhancing the proliferation, adhesion, and spreading of WJMSCs. Moreover, the LiCS cement exhibited profound immunomodulatory effects, as evidenced by the reduction of pro-inflammatory cytokines and the promotion of macrophage polarization towards the anti-inflammatory M2 phenotype. This dual function was further supported by enhanced osteogenic differentiation, as indicated by elevated levels of alkaline phosphatase and osteocalcin expression. These comprehensive *in vitro* results highlight the potential of LiCS cement as a dual-action material capable of orchestrating osteogenesis and immune modulation. Thus, LiCS cement is a promising candidate for bone tissue engineering and regeneration. *In vivo* studies are essential to validate these promising findings

and fully elucidate the clinical potential of LiCS cement in bone repair and regenerative applications.

Acknowledgements

Experiments and data analyses were performed in part by the Medical Research Core Facilities, Office of Research & Development, China Medical University, Taichung, Taiwan.

Author contributions

Yen-Hong Lin: Methodology, Investigation, Writing-Original draft preparation; Cheng-Yu Chen: Methodology, Investigation; Kun-Hao Chen: Methodology, Investigation; Ting-You Kuo: Methodology, Investigation; Tsung-Li Lin: Methodology, Investigation, Writing-Original draft preparation and Editing; Ming-You Shie: Writing-Reviewing and Editing.

Funding

The authors acknowledge receipt of a grant from the National Science and Technology Council (NSTC 113-2314-B-039-053, 112-2628-E-039-001-MY3, and 113-2811-E-039-001) of Taiwan, and China Medical University Hospital grants (DMR-113-076) of Taiwan.

Data availability

No datasets were generated or analysed during the current study.

Declarations

Ethics approval and consent to participate

Not applicable.

Consent for publication

Not applicable.

Competing interests

The authors declare no competing interests.

Received: 23 May 2024 / Accepted: 8 November 2024

Published online: 06 January 2025

References

1. Sheng X, Li C, Wang Z, Xu Y, Sun Y, Zhang W, et al. Advanced applications of strontium-containing biomaterials in bone tissue engineering. *Mater Today Bio*. 2023;20:100636.
2. Su Z, Guo C, Gui X, Wu L, Zhang B, Qin Y, et al. 3D printing of customized bioceramics for promoting bone tissue regeneration by regulating sympathetic nerve behavior. *J Mater Chem B*. 2024;12:4217–31.
3. Luo S, Wang Z, He J, Tang G, Yuan D, Wu Z, et al. Bioceramic modular tissue-engineered bone with rapid vascularization for large bone defects. *Ceram Int*. 2024;50:18275–83.
4. Ma C, Tao C, Zhang Z, Zhou H, Fan C, Wang D. Development of artificial bone graft via *in vitro* endochondral ossification (ECO) strategy for bone repair. *Mater Today Bio*. 2023;23:100893.
5. Chen YT, Chuang YH, Chen CM, Wang JY, Wang J. Development of hybrid scaffolds with biodegradable polymer composites and bioactive hydrogels for bone tissue engineering. *Biomater Adv*. 2023;153:213562.
6. Chen YW, Lin YH, Lin TL, Lee KX, Yu MH, Shie MY. 3D-biofabricated chondrocyte-laden decellularized extracellular matrix-contained gelatin methacrylate auxetic scaffolds under cyclic tensile stimulation for cartilage regeneration. *Biofabrication*. 2023;15:045007.
7. Han X, Wang F, Ma Y, Lv X, Zhang K, Wang Y, et al. TPG-functionalized PLGA/PCL nanofiber membrane facilitates periodontal tissue regeneration by modulating macrophages polarization via suppressing PI3K/AKT and NF- κ B signaling pathways. *Mater Today Bio*. 2024;26:101036.
8. Lukin I, Erezuma I, Desimone MF, Zhang YS, Dolatshahi-Pirouz A, Orive G. Nanomaterial-based drug delivery of immunomodulatory factors for bone and cartilage tissue engineering. *Biomater Adv*. 2023;154:213637.
9. Chen Z, Xing F, Zhou Y, Yu P, Xu J, Luo R, et al. Integrated osteoimmunomodulatory strategies based on designing scaffold surface properties in bone regeneration. *J Mater Chem B*. 2023;11:6718–45.

10. Wang M, Chen F, Tang Y, Wang J, Chen X, Li X, et al. Regulation of macrophage polarization and functional status by modulating hydroxyapatite ceramic micro/nano-topography. *Mater Des.* 2022;213:110302.
11. Carrara SC, Davila-Lezama A, Cabriel C, Berenschot EJW, Krol S, Gardeniers JGE, et al. 3D topographies promote macrophage M2-subset differentiation. *Mater Today Bio.* 2024;24:100897.
12. Luo Y, Yang Z, Zhao X, Li D, Li Q, Wei Y, et al. Immune regulation enhances osteogenesis and angiogenesis using an injectable thiolated hyaluronic acid hydrogel with lithium-doped nano-hydroxyapatite (Li-nHA) delivery for osteonecrosis. *Mater Today Bio.* 2024;25:100976.
13. Pan X, Ou M, Lu Y, Nie Q, Dai X, Liu O. Immunomodulatory zinc-based materials for tissue regeneration. *Biomater Adv.* 2023;152:213503.
14. Song Z, Cheng Y, Chen M, Xie X. Macrophage polarization in bone implant repair: a review. *Tissue Cell.* 2023;82:102112.
15. Hu Y, Tang L, Wang Z, Yan H, Yi X, Wang H, et al. Inducing in situ M2 macrophage polarization to promote the repair of bone defects via scaffold-mediated sustained delivery of luteolin. *J Control Release.* 2024;365:889–904.
16. Ali M, He Y, Chang ASN, Wu A, Liu J, Cao Y, et al. Osteoimmune-modulating and BMP-2-eluting anodised 3D printed titanium for accelerated bone regeneration. *J Mater Chem B.* 2023;12:97–111.
17. Shie MY, Ding SJ. Integrin binding and MAPK signal pathways in primary cell responses to surface chemistry of calcium silicate cements. *Biomaterials.* 2013;34:6589–606.
18. Tsai YL, Lee JJ, Wang CY, Lin YH, Chen CY, Shie MY. Gallic acid-coated nanolayer on mineral trioxide aggregate for regulating the inflammatory and differentiation cellular response profile of human dental pulp stem cells. *Ceram Int.* 2024;50:14656–63.
19. Lin YH, Chuang TY, Chiang WH, Chen IWP, Wang K, Shie MY, et al. The synergistic effects of graphene-contained 3D-printed calcium silicate/poly- ϵ -caprolactone scaffolds promote FGFR-induced osteogenic/angiogenic differentiation of mesenchymal stem cells. *Mater Sci Eng C.* 2019;104:109887.
20. Kao CT, Chiu YC, Lee AKX, Lin YH, Huang TH, Liu YC, et al. The synergistic effects of Xu Duan combined Sr-contained calcium silicate/poly- ϵ -caprolactone scaffolds for the promotion of osteogenesis marker expression and the induction of bone regeneration in osteoporosis. *Mater Sci Eng C.* 2021;119:111629.
21. Chiu YC, Lin YH, Chen YW, Kuo TY, Shie MY. Additive manufacturing of barium-doped calcium silicate/poly- ϵ -caprolactone scaffolds to activate CaSR and AKT signalling and osteogenic differentiation of mesenchymal stem cells. *J Mater Chem B.* 2023;11:4666–76.
22. Li J, Li J, Wei Y, Xu N, Li J, Pu X, et al. Ion release behavior of vanadium-doped mesoporous bioactive glass particles and the effect of the released ions on osteogenic differentiation of BMSCs via the FAK/MAPK signaling pathway. *J Mater Chem B.* 2021;9:7848–65.
23. Zhang X, Cui J, Cheng L, Lin K. Enhancement of osteoporotic bone regeneration by strontium-substituted 45S5 bioglass via time-dependent modulation of autophagy and the Akt/mTOR signaling pathway. *J Mater Chem B.* 2021;9:3489–501.
24. Shie MY, Ding SJ, Chang HC. The role of silicon in osteoblast-like cell proliferation and apoptosis. *Acta Biomater.* 2011;7:2604–14.
25. Wu M, Chen F, Liu H, Wu P, Yang Z, Zhang Z, et al. Bioinspired sandwich-like hybrid surface functionalized scaffold capable of regulating osteogenesis, angiogenesis, and osteoclastogenesis for robust bone regeneration. *Mater Today Bio.* 2022;17:100458.
26. Zhang Q, Gao S, Li B, Li Q, Li X, Cheng J, et al. Lithium-doped titanium dioxide-based multilayer hierarchical structure for accelerating nerve-induced bone regeneration. *ACS Appl Mater Interfaces.* 2024;16:22887–99.
27. Liu L, Yu F, Chen L, Xia L, Wu C, Fang B. Lithium-containing biomaterials stimulate cartilage repair through bone marrow stromal cells-derived exosomal miR-455-3p and histone H3 acetylation. *Adv Healthc Mater.* 2023;12:2202390.
28. Salam N, Gibson IR. Lithium ion doped carbonated hydroxyapatite compositions: synthesis, physicochemical characterisation and effect on osteogenic response in vitro. *Biomater Adv.* 2022;140:213068.
29. Zhu Z, Yin J, Guan J, Hu B, Niu X, Jin D, et al. Lithium stimulates human bone marrow derived mesenchymal stem cell proliferation through GSK-3 β -dependent β -catenin/Wnt pathway activation. *FEBS J.* 2014;281:5371–89.
30. Wang W, Wei J, Lei D, Wang S, Zhang B, Shang S, et al. 3D printing of lithium osteogenic bioactive composite scaffold for enhanced bone regeneration. *Compos Part B Eng.* 2023;256:110641.
31. Alicka M, Sobierajska P, Kornicka K, Wiglusz RJ, Marycz K. Lithium ions (Li+) and nanohydroxyapatite (nHA) doped with Li+ enhance expression of late osteogenic markers in adipose-derived stem cells. Potential theranostic application of nHA doped with Li+ and co-doped with europium (III) and samarium (III) ions. *Mater Sci Eng C.* 2019;99:1257–73.
32. Wang CY, Chen CY, Chen KH, Lin YH, Yeh TP, Lee AKX, et al. The synergistic effects of strontium/magnesium-doped calcium silicate cement accelerates early angiogenesis and bone regeneration through double bioactive ion stimulation. *Ceram Int.* 2024;50:7121–31.
33. Zhang F, Zhou M, Gu W, Shen Z, Ma X, Lu F, et al. Zinc-/copper-substituted dicalcium silicate cement: advanced biomaterials with enhanced osteogenesis and long-term antibacterial properties. *J Mater Chem B.* 2020;8:1060–70.
34. Xu Z, Zhang D, Li H, Yin L, Song H, Wang W, et al. Effects of additives on the mechanical properties, rheology, and printing properties of Pcc-based 3DPMs. *Ceram Int.* 2023;49:28354–68.
35. Mansoori-Kermani A, Mashayekhan S, Kermani F, Abdekhodaie MJ. The effect of tricalcium silicate incorporation on bioactivity, injectability, and mechanical properties of calcium sulfate/bioactive glass bone cement. *Ceram Int.* 2023;49:15003–14.
36. Zhao W, Wang J, Zhai W, Wang Z, Chang J. The self-setting properties and in vitro bioactivity of tricalcium silicate. *Biomaterials.* 2005;26:6113–21.
37. Zareidoost A, Yousefpour M, Ghaseme B, Amanzadeh A. The relationship of surface roughness and cell response of chemical surface modification of titanium. *J Mater Sci Mater Med.* 2012;23:1479–88.
38. Keikhosravani P, Maleki-Ghaleh H, Khosrowshahi AK, Bodaghi M, Dargahi Z, Kavanlouei M, et al. Bioactivity and antibacterial behaviors of nanostructured lithium-doped hydroxyapatite for bone scaffold application. *Int J Mol Sci.* 2021;22:9214.
39. Lin TL, Lin YH, Lee AKX, Kuo TY, Chen CY, Chen KH, et al. The exosomal secretomes of mesenchymal stem cells extracted via 3D-printed lithium-doped calcium silicate scaffolds promote osteochondral regeneration. *Mater Today Bio.* 2023;22:100728.
40. Liu WC, Hu CC, Tseng YY, Sakthivel R, Fan KS, Wang AN, et al. Study on strontium doped tricalcium silicate synthesized through sol-gel process. *Mater Sci Eng C.* 2020;108:110431.
41. Zhang NZ, Zhang M, Tang HY, Qin L, Cheng CK. P2O5 enhances the bioactivity of lithium silicate glass ceramics via promoting phase transformation and forming Li3PO4. *Ceram Int.* 2024;50:13308–17.
42. Kokubo T. Bioactive glass ceramics: properties and applications. *Biomaterials.* 1991;12:155–63.
43. Mass E, Nimmerjahn F, Kierdorf K, Schlitzer A. Tissue-specific macrophages: how they develop and choreograph tissue biology. *Nat Rev Immunol.* 2023;23:563–79.
44. Deng C, Chang J, Wu C. Bioactive scaffolds for osteochondral regeneration. *J Orthop Translat.* 2019;17:15–25.
45. Wu Z, Bai J, Ge G, Wang T, Feng S, Ma Q, et al. Regulating macrophage polarization in high glucose microenvironment using lithium-modified bioglass-hydrogel for diabetic bone regeneration. *Adv Healthc Mater.* 2022;11:2200298.
46. Haxaire C, Hay E, Geoffroy V. Runx2 controls bone resorption through the down-regulation of the wnt pathway in osteoblasts. *Am J Pathol.* 2016;186:1598–609.
47. Noble W, Planel E, Zehr C, Olm V, Meyerson J, Suleman F, et al. Inhibition of glycogen synthase kinase-3 by lithium correlates with reduced tauopathy and degeneration in vivo. *Proc Natl Acad Sci.* 2005;102:6990–5.
48. Zhai D, Chen L, Chen Y, Zhu Y, Xiao Y, Wu C. Lithium silicate-based bioceramics promoting chondrocyte maturation by immunomodulating M2 macrophage polarization. *Biomater Sci.* 2020;8:4521–34.
49. Monteiro NO, Casanova MR, Quinteira R, Figueiro JF, Reis RL, Neves NM. Biomimetic surface topography as a potential modulator of macrophages inflammatory response to biomaterials. *Biomater Adv.* 2022;141:213128.
50. Cheng G, Guo S, Li M, Xiao S, Jiang B, Ding Y. Hydroxyapatite-coated small intestinal submucosa membranes enhanced periodontal tissue regeneration through immunomodulation and osteogenesis via BMP-2/Smad signaling pathway. *Adv Healthc Mater.* 2024;13:e2301479.

Publisher's note

Springer Nature remains neutral with regard to jurisdictional claims in published maps and institutional affiliations.